An algorithm for total variation regularized photoacoustic imaging

Yiqiu Dong · Torsten Görner · Stefan Kunis

Abstract Recovery of image data from photoacoustic measurements asks for the inversion of the spherical mean value operator. In contrast to direct inversion methods for specific geometries, we consider a semismooth Newton scheme to solve a total variation regularized least squares problem. During the iteration, each matrix vector multiplication is realized in an efficient way using a recently proposed spectral discretization of the spherical mean value operator. All theoretical results are illustrated by numerical experiments.

Key words and phrases : spherical mean operator, fast Fourier transform, total variation regularization, photoacoustic imaging.

2010 AMS Mathematics Subject Classification : 65T50, 44A12, 92C55.

1 Introduction

Analogously to the inversion of the Radon transform in computerized tomography, recovering a function from its mean values over a family of spheres is the crucial ingredient in photoacoustic imaging [40, 25, 6]. The recovery of a function from such spherical means has been studied recently in [11, 3, 1, 25, 36] and references therein. In all practical applications the so called center points are located on a fixed measurement curve or surface and for specific geometries, direct reconstruction algorithms are discussed in [18, 29, 28, 17, 2, 10, 27, 13, 4]. Generalizations to integrating detectors and to variable speed of sound, having no direct relation to the spherical mean value operator, are studied in [16, 7, 33, 43, 19, 42] and [22, 39, 35], respectively.

In this paper we consider constant speed of sound and center points located on an arbitrary curve or surface. For this situation, the reconstruction problem is known to be ill-posed, see e.g. [25, 32] for a detailed discussion, and it has been pointed out recently that direct reconstruction formulae are out of reach, cf. [30, 15, 14]. We regularize the original problem by a total variation (TV) term with the aim of preserving significant edges in the reconstructed images [37]. We set up an iterative method to solve the total variation regularized least squares problem based on the Fenchel-Rockafellar-duality and inexact semismooth Newton techniques following the approach in [21]. In each iteration, we apply the recently proposed algorithm [12] for the fast and accurate computation of spherical means.

Yiqiu Dong
Technical University of Denmark, Department of Applied Mathematics and Computer Science, yido@dtu.dk

Torsten Görner
University Osnabrück, Institute of Mathematics, torsten.goerner@uos.de

Stefan Kunis
University Osnabrück, Institute of Mathematics, and Helmholtz Zentrum München, stefan.kunis@math.uos.de

The structure of our paper is as follows. Section 2 reviews the Cauchy problem for the wave equation and its relation to the spherical mean value operator. After discretization of this operator via trigonometric polynomials, we discuss the algorithmic properties of this discrete spherical mean value operator. The following section sets up the total variation regularized least squares problem (P_0) and studies a tight relaxation for which the semismooth Newton method [34, 20] is applied. Several numerical experiments are reported in Section 4 and we conclude our findings in the last section.

2 Photoacoustic imaging, spherical means, and discretization

In many topics of photoacoustic imaging we have to deal with the Cauchy problem for the wave equation

$$
\begin{aligned}
\partial_t^2 p(\boldsymbol{x}, t) - \nu_s^2(\boldsymbol{x}) \Delta p(\boldsymbol{x}, t) = 0 & \quad \text{for } (\boldsymbol{x}, t) \in \mathbb{R}^d \times (0, \infty), \\
p(\boldsymbol{x}, 0) = f(\boldsymbol{x}) & \quad \text{for } \boldsymbol{x} \in \mathbb{R}^d, \\
\partial_t p(\boldsymbol{x}, 0) = 0 & \quad \text{for } \boldsymbol{x} \in \mathbb{R}^d,
\end{aligned}
\tag{1}
$$

where $d \in \mathbb{N}$, $d \geq 2$, is the spatial dimension, p is the pressure and ν_s is the speed of sound within the medium. In general, the speed of sound depends on the spatial variable $\boldsymbol{x}$, but we assume for simplicity homogeneity and after rescaling suppose $\nu_s = 1$. Otherwise, photoacoustic imaging has no direct relation to the spherical mean value operator and other methods [22, 39, 35] have been considered. It is well-known that for a sufficiently smooth function $f : \mathbb{R}^d \to \mathbb{R}$ the solution of (1) can be given as

$$
p(\boldsymbol{x}, t) = \begin{cases}
\frac{1}{\Gamma\left(\frac{d}{2}\right) 2^{\frac{d-2}{2}}} \frac{\partial}{\partial t} \left(t^{-1} \frac{\partial}{\partial t}\right)^{\frac{d-2}{2}} \int_0^t \frac{r}{\sqrt{t^2 - r^2}} r^{d-2} \left(\mathcal{M}f\right)(\boldsymbol{x}, r) \, \mathrm{d}r & \text{for even } d, \\
\frac{\sqrt{\pi}}{\Gamma\left(\frac{d}{2}\right) 2^{\frac{d-1}{2}}} \frac{\partial}{\partial t} \left(t^{-1} \frac{\partial}{\partial t}\right)^{\frac{d-3}{2}} \left(t^{d-2} \left(\mathcal{M}f\right)(\boldsymbol{x}, t)\right) & \text{for odd } d,
\end{cases}
$$

see [9, §VI.13, eq. 13-15], where the spherical mean value operator $\mathcal{M}$ is defined by

$$
\mathcal{M}f(\boldsymbol{x}, r) := \frac{1}{\omega_{d-1}} \int_{\mathbb{S}^{d-1}} f(\boldsymbol{x} + r\boldsymbol{\xi}) \mathrm{d}\sigma(\boldsymbol{\xi}), \quad (\boldsymbol{x}, r) \in \mathbb{R}^d \times (0, \infty).
$$

Here, $\mathbb{S}^d := \{\boldsymbol{x} \in \mathbb{R}^d : |\boldsymbol{x}|_2^2 := \sum_{j=1}^d x_j^2 = 1\}$ denotes the $d - 1$ dimensional sphere, σ denotes the surface measure on $\mathbb{S}^{d-1}$ and $\omega_{d-1} := \sigma(\mathbb{S}^{d-1})$.

The goal is to recover f from measurements $p(\boldsymbol{y}, t)$, $(\boldsymbol{y}, t) \in \Omega \times \mathbb{R}$, where $\Omega \subset \mathbb{R}^d$ is some manifold surrounding the region of interest. In particular for spatial dimension $d = 3$, we have to find $f(\boldsymbol{x})$, $\boldsymbol{x} \in \mathbb{R}^3$, from the data

$$
p(\boldsymbol{y}, t) = \frac{\partial}{\partial t} \left(t \left(\mathcal{M}f\right)(\boldsymbol{y}, t)\right), \quad \boldsymbol{y} \in \Omega \subset \mathbb{R}^3, \quad t \in \mathbb{R}.
$$

In this paper, we limit our considerations to recover a function from its spherical means with iterative methods. For this purpose, the efficient and accurate computation of spherical means from given function values on some grid is essential. We follow our recent approach in [12], consider functions supported in a subset of $[-\frac{1}{2}, \frac{1}{2}]^d =: \mathbb{T}^d$ and approximate these by trigonometric polynomials. Moreover, we assume that the manifold $\Omega \subset \mathbb{T}^d$ and the support of the function fulfill $\sup\{|\boldsymbol{y} - \boldsymbol{x}|_2 : \boldsymbol{y} \in \Omega, \boldsymbol{x} \in \mathrm{supp}f\} \leq 1$, and we thus can restrict the radii to $r \leq 1$. The spherical mean value operator is bounded from $L^p(\mathbb{T}^d)$ to $L^p(\mathbb{T}^d \times [0, 1], \mathrm{d}\boldsymbol{y} r^{d-1} \mathrm{d}r)$ and for a fixed radius r, the complex exponential functions $e_{\boldsymbol{k}} : \mathbb{R}^d \to \mathbb{C}$, $e_{\boldsymbol{k}}(\boldsymbol{x}) := \mathrm{e}^{2\pi \mathrm{i} \boldsymbol{k} \boldsymbol{x}}$, $\boldsymbol{k} \in \mathbb{Z}^d$, are eigenfunctions in the sense

$$
\mathcal{M}e_{\boldsymbol{k}}(\boldsymbol{y}, r) = e_{\boldsymbol{k}}(\boldsymbol{y}) \frac{\Gamma\left(\frac{d}{2}\right) \mathrm{J}_{\frac{d-2}{2}}(2\pi|\boldsymbol{k}|_2 r)}{(\pi|\boldsymbol{k}|_2 r)^{\frac{d-2}{2}}},
$$

where J_ν denotes the Bessel function of first kind with order ν. For some discretization parameter $n \in \mathbb{N}$, the function $f : \mathbb{T}^d \to \mathbb{R}$ is typically given by discrete values $f(\boldsymbol{x})$ on a regular grid $\boldsymbol{x} \in X \subset \mathbb{T}^d$,

$$X := \left\{ \left(\tfrac{2j_1+1-n}{2n}, \ldots, \tfrac{2j_d+1-n}{2n} \right)^\top : \boldsymbol{j} \in \{0, \ldots, n-1\}^d \right\},$$

and the spherical means $\mathcal{M}f(\boldsymbol{y}, r)$ have to be computed for scattered center points $\boldsymbol{y} \in Y \subset \Omega$ and radii $r \in R \subset [0,1]$, where $M_1, M_2 \in \mathbb{N}$ denote the cardinalities of these sets. To this end, we compute discrete Fourier coefficients

$$\hat{f}_{\boldsymbol{k}} := \frac{1}{n^d} \sum_{\boldsymbol{x} \in X} f(\boldsymbol{x}) \mathrm{e}^{-2\pi \mathrm{i} \boldsymbol{k} \boldsymbol{x}}, \quad \boldsymbol{k} \in J_n := \left[-\frac{n}{2}, \frac{n}{2} \right)^d \cap \mathbb{Z}^d,$$

by one ordinary fast Fourier transform (FFT) in the first step. Subsequently, we compute for each radius $r \in R$ auxiliary coefficients

$$\tilde{h}_{\boldsymbol{k},r} := \hat{f}_{\boldsymbol{k}} \frac{\Gamma\left(\frac{d}{2}\right) \mathrm{J}_{\frac{d-2}{2}}(2\pi |\boldsymbol{k}|_2 r)}{(\pi |\boldsymbol{k}|_2 r)^{\frac{d-2}{2}}}, \quad \boldsymbol{k} \in J_n,$$

and evaluate

$$\mathcal{M}f(\boldsymbol{y}, r) \approx g(\boldsymbol{y}, r) := \sum_{\boldsymbol{k} \in J_n} \tilde{h}_{\boldsymbol{k},r} \mathrm{e}^{2\pi \mathrm{i} \boldsymbol{k} \boldsymbol{y}}, \quad \boldsymbol{y} \in Y,$$

by nonequispaced FFTs. In matrix vector notation, this sums up to

$$\boldsymbol{g} = \boldsymbol{M} \boldsymbol{f},$$

with a discrete spherical mean value operator $\boldsymbol{M} : \mathbb{R}^N \to \mathbb{C}^M$, $N := n^d$, $M := M_1 M_2$,

$$\boldsymbol{M} := \begin{pmatrix} \boldsymbol{A} \boldsymbol{D}_1 \boldsymbol{F} \\ \boldsymbol{A} \boldsymbol{D}_2 \boldsymbol{F} \\ \vdots \\ \boldsymbol{A} \boldsymbol{D}_{M_2} \boldsymbol{F} \end{pmatrix},$$

with the following nonequispaced Fourier matrix $\boldsymbol{A} \in \mathbb{C}^{M_1 \times N}$, diagonal matrices $\boldsymbol{D}_j \in \mathbb{R}^{N \times N}$, $j = 1, \ldots, M_2$, and a Fourier matrix $\boldsymbol{F} \in \mathbb{C}^{N \times N}$,

$$\begin{aligned} (\boldsymbol{A})_{\boldsymbol{y}, \boldsymbol{k}} &:= \mathrm{e}^{2\pi \mathrm{i} \boldsymbol{k} \boldsymbol{y}}, & \boldsymbol{y} \in Y, \boldsymbol{k} \in J_n, \\ (\boldsymbol{D}_j)_{\boldsymbol{k}, \boldsymbol{k}} &:= \frac{\Gamma\left(\frac{d}{2}\right) \mathrm{J}_{\frac{d-2}{2}}(2\pi |\boldsymbol{k}|_2 r_j)}{(\pi |\boldsymbol{k}|_2 r_j)^{\frac{d-2}{2}}}, & \boldsymbol{k} \in J_n, \\ (\boldsymbol{F})_{\boldsymbol{k}, \boldsymbol{x}} &:= \mathrm{e}^{-2\pi \mathrm{i} \boldsymbol{k} \boldsymbol{x}}, & \boldsymbol{k} \in J_n, \boldsymbol{x} \in X. \end{aligned}$$

An immediate consequence is given by

Lemma 1 *With the above definitions, we have*

$$\boldsymbol{M}^* \boldsymbol{M} = \boldsymbol{F}^* \left(\sum_{j=1}^{M_2} \boldsymbol{D}_j \boldsymbol{T} \boldsymbol{D}_j \right) \boldsymbol{F}$$

with the Hermitian multilevel Toeplitz matrix $\boldsymbol{T} \in \mathbb{C}^{N \times N}$,

$$(\boldsymbol{T})_{\boldsymbol{k}, \boldsymbol{l}} := \sum_{\boldsymbol{y} \in Y} \mathrm{e}^{2\pi \mathrm{i} (\boldsymbol{k} - \boldsymbol{l}) \boldsymbol{y}}.$$

Proof We rewrite the above definition as

$$M = \begin{pmatrix} A & & \\ & \ddots & \\ & & A \end{pmatrix} \begin{pmatrix} D_1 \\ \vdots \\ D_{M_2} \end{pmatrix} F$$

and use

$$(A^*A)_{k,l} = \sum_{y \in Y} e^{2\pi i (k-l)y}$$

Due to Lemma 1, we conclude the following sufficient conditions on the regularity of the matrix M^*M. If the radii r_j, $j = 1, \ldots, M_2$, are chosen in such a way that the diagonal matrices D_j are regular and the center points $y \in Y$ are in general position for the multivariate trigonometric interpolation problem of degree n, then M^*M is strictly positive definite. In particular, it suffices to choose an arbitrary curve or manifold $\Omega \subset \mathbb{T}^d$, such that no nonzero trigonometric polynomial of degree n vanishes, and sample center points $Y \subset \Omega$ dense enough. However note that this asks for at least n^d center points which is an order of magnitude to large and this will not overcome the ill-conditioning of the discrete problem. Subsequently, we assume that M^*M is invertible.

As detailed in [12], the above approach leads to an algorithm of complexity $\mathcal{O}(M_2(N \log N + M_1))$ in general using the nonequispaced FFT [24]. For the two-dimensional case, i.e. $n \times n$ images, $M_1 = M_2 = \mathcal{O}(n)$ detectors and radii, this leads to a semi-fast method of complexity $\mathcal{O}(n^3 \log n)$. In case $d = 3$, i.e. $n \times n \times n$ volumes, $M_1 = \mathcal{O}(n^2)$ detectors and $M_2 = \mathcal{O}(n)$ radii, the FFT-based algorithm can be improved by the recently proposed butterfly sparse FFT [41, 26] and leads to an algorithm of complexity $\mathcal{O}(n^3 \log n)$.

We note in passing that the considered trigonometric interpolation is complex valued also for real valued functions, but can easily be made real valued by extending the discrete Fourier coefficients $\hat{f}_k$ to $\{-\frac{n}{2}, \ldots, \frac{n}{2}\}^d \supset J_n$ appropriately. Subsequently, we consider this real valued discrete spherical mean value operator in the two-dimensional case for ease of notation.

3 TV-based iterative method

We now turn to the reconstruction problem

$$Mf = g, \tag{2}$$

where $g \in \mathbb{R}^M$ is the vector of discrete spherical mean values, $f \in \mathbb{R}^N$ is a real valued image obtained from a two-dimensional n-by-n pixel-array on a regular grid by concatenation in the usual columnwise fashion with $N = n^2$, and $M \in \mathbb{R}^{M \times N}$ is the discrete spherical mean value operator. We assume that M^*M is invertible and will add a small multiple of the identity matrix if this is not the case. The problem of reconstructing the image f from the measurements g is known to be ill-posed. Hence, regularization techniques based on a prior information on f are utilized to get a stable reconstruction process. The total variation (TV) seminorm, having great success in image restoration [37], is defined by

$$\|v\|_{\text{TV}} := \sum_{j=1}^N |[\nabla v]_j|_2 = \sum_{j=1}^N \sqrt{|(\nabla_x v)_j|^2 + |(\nabla_y v)_j|^2}.$$

Here, we use the abbreviation $[p]_j = (p_j, p_{N+j})^\top$, $p \in \mathbb{R}^{2N}$, $j = 1, \ldots, N$, and define the discrete gradient operator $\nabla \in \mathbb{R}^{2N \times N}$ by $[\nabla v]_j := ((\nabla_x v)_j, (\nabla_y v)_j)^\top$ with the forward differences and symmetric boundary conditions in the respective coordinate directions, i.e.,

$$(\nabla_x v)_j := \begin{cases} v_{s+1,t} - v_{s,t}, & \text{if } s < n, \\ 0, & \text{if } s = n, \end{cases} \qquad (\nabla_y v)_j := \begin{cases} v_{s,t+1} - v_{s,t}, & \text{if } t < n, \\ 0, & \text{if } t = n, \end{cases}$$

where $j = sn + t$ with $(s, t) \in \{1, 2, \cdots, n\} \times \{1, 2, \cdots, n\}$ is an index in the regular pixel-array. Combining the TV regularization with an l^2-data-fitting term, we reconstruct the image $\boldsymbol{f}$ by solving the minimization problem

$$\min_{\boldsymbol{f} \in \mathbb{R}^N} \mathcal{J}(\boldsymbol{f}), \quad \mathcal{J}(\boldsymbol{f}) := \frac{1}{2} \|\boldsymbol{M}\boldsymbol{f} - \boldsymbol{g}\|_2^2 + \alpha \|\boldsymbol{f}\|_{\mathrm{TV}}, \tag{P_0}$$

where $\alpha > 0$ is the regularization parameter to control the trade-off between a good fitness to the data $\boldsymbol{g}$ and the smoothness from the TV term.

The TV term is nondifferentiable and this is responsible for preserving edges in images but also poses an algorithmic challenge. Such a nondifferentiability conforms with the nonuniqueness to solutions of its Fenchel-Rockafellar-dual, see [21] for more details. In order to overcome the difficulty, referring to [21, 31] we propose a dual regularization in the Fenchel-Rockafellar-dual of (P_0), (P^*), and correspondingly obtain a local smoothness of the nondifferentiable TV term, i.e.,

$$\sup_{\boldsymbol{p} \in \mathbb{R}^{2N}} -\frac{1}{2} \|\boldsymbol{M}^* \boldsymbol{g} - \mathrm{div}\boldsymbol{p}\|_{\boldsymbol{M}}^2 + \frac{1}{2} \|\boldsymbol{g}\|_2^2 - \frac{\gamma}{2\alpha} \sum_{j=1}^{N} |[\boldsymbol{p}]_j|_2^2,$$

$$\text{subject to (s.t.) } |[\boldsymbol{p}]_j|_2 \leq \alpha \text{ for } j = 1, \ldots, N, \tag{P^*}$$

$$\min_{\boldsymbol{f} \in \mathbb{R}^N} \frac{1}{2} \|\boldsymbol{M}\boldsymbol{f} - \boldsymbol{g}\|_2^2 + \sum_{j=1}^{N} (\Phi_\gamma(\nabla \boldsymbol{f}))_j, \tag{P}$$

where $\boldsymbol{p} \in \mathbb{R}^{2N}$ is the dual variable, we have $\|\boldsymbol{v}\|_{\boldsymbol{M}}^2 := \langle (\boldsymbol{M}^*\boldsymbol{M})^{-1}\boldsymbol{v}, \boldsymbol{v} \rangle = \sum_{j=1}^{N} \boldsymbol{v}_j \cdot ((\boldsymbol{M}^*\boldsymbol{M})^{-1}\boldsymbol{v})_j$, the divergence operator is given by $\mathrm{div} = -\nabla^*$, $\gamma > 0$ is the dual regularization parameter, and $\Phi_\gamma : \mathbb{R}^{2N} \to \mathbb{R}^N$ is defined by

$$(\Phi_\gamma(\nabla \boldsymbol{f}))_j := \begin{cases} \frac{\alpha}{2\gamma} \left|[\nabla \boldsymbol{f}]_j\right|_2^2, & \text{if } \left|[\nabla \boldsymbol{f}]_j\right|_2 < \gamma, \\ \alpha \left(\left|[\nabla \boldsymbol{f}]_j\right|_2 - \frac{\gamma}{2} \right), & \text{if } \left|[\nabla \boldsymbol{f}]_j\right|_2 \geq \gamma. \end{cases}$$

Here, Φ_γ is a Huber function [23], which smooths locally the TV term in order to obtain the differentiability of (P_0) and the uniqueness of the dual solution $\boldsymbol{p}$. In Φ_γ, the parameter γ controls the trade-off between quadratic regularization and the TV regularization. Roughly speaking, large γ leads to smoothing of edges and benefits the numerical computation. On the other hand, small γ leads to good edge preservation due to the non-differentiability of the TV regularization. In addition, referring to Theorem 2.2 in [21], we have the following result.

Theorem 1 *Suppose $\bar{\boldsymbol{f}}_\gamma$ is the solution of (P) and $\bar{\boldsymbol{f}}$ is the solution of (P_0). Then, as $\gamma \to 0$, $\bar{\boldsymbol{f}}_\gamma$ converges to $\bar{\boldsymbol{f}}$.*

Based on the first order optimality condition, the solutions $\bar{\boldsymbol{f}}_\gamma$ and $\bar{\boldsymbol{p}}_\gamma$ of (P) and (P^*), respectively, satisfy

$$\boldsymbol{M}^*\boldsymbol{M}\bar{\boldsymbol{f}}_\gamma + \mathrm{div}\bar{\boldsymbol{p}}_\gamma = \boldsymbol{M}^*\boldsymbol{g}, \tag{3}$$

$$\max\{\gamma, |[\nabla \bar{\boldsymbol{f}}_\gamma]_j|_2\}[\bar{\boldsymbol{p}}_\gamma]_j = -\alpha[\nabla \bar{\boldsymbol{f}}_\gamma]_j, \qquad \text{for } j = 1, \ldots, N.$$

Due to the presence of the max-operator, the system is not smooth but semismooth. We solve it by the semismooth Newton technique, see [34, 20], and each semismooth Newton step is given by

$$\boldsymbol{f}^{l+1} := \boldsymbol{f}^l + \boldsymbol{\delta}_f \text{ with } \boldsymbol{H}^l \boldsymbol{\delta}_f = \boldsymbol{w}^l \tag{4}$$

$$\boldsymbol{p}^{l+1} := \boldsymbol{p}^l + \boldsymbol{\delta}_p = -\boldsymbol{D}(\boldsymbol{m}_{\gamma^l})^{-1} \left[\alpha \nabla \boldsymbol{f}^{l+1} + \chi_{\mathcal{A}^l} \boldsymbol{D}(\boldsymbol{p}^l) \boldsymbol{N}(\nabla \boldsymbol{f}^l) \nabla \boldsymbol{\delta}_f \right] \tag{5}$$

with

$$\boldsymbol{H}^l := \boldsymbol{M}^*\boldsymbol{M} + \nabla^* \boldsymbol{D}(\boldsymbol{m}_{\gamma^l})^{-1} \left[\alpha \boldsymbol{I}_N + \chi_{\mathcal{A}^l} \boldsymbol{D}(\boldsymbol{p}^l) \boldsymbol{N}(\nabla \boldsymbol{f}^l) \right] \nabla,$$

$$\boldsymbol{w}^l := -\boldsymbol{M}^*(\boldsymbol{M}\boldsymbol{f}^l - \boldsymbol{g}) - \alpha\nabla^*\boldsymbol{D}(\boldsymbol{m}_{\gamma^l})^{-1}\nabla\boldsymbol{f}^l.$$

Here, $\boldsymbol{I}_N \in \mathbb{R}^{N \times N}$ is the identity matrix, $\boldsymbol{D}(\boldsymbol{m}_{\gamma^l}) \in \mathbb{R}^{2N \times 2N}$ is a diagonal matrix with the vector $\boldsymbol{m}_{\gamma^l} \in \mathbb{R}^{2N}$, $(\boldsymbol{m}_{\gamma^l})_j = (\boldsymbol{m}_{\gamma^l})_{N+j} = \max\{\gamma, |[\nabla\boldsymbol{f}^l]_j|_2\}$, as the main diagonal. Moreover, we define the set $\mathcal{A}^l = \{j : |[\nabla\boldsymbol{f}^l]_j|_2 > \gamma\}$ and the thresholding operator as diagonal matrix $\chi_{\mathcal{A}} \in \mathbb{R}^{2N \times 2N}$,

$$(\chi_{\mathcal{A}})_{j,j} := (\chi_{\mathcal{A}})_{N+j,N+j} := \begin{cases} 1, \text{ if } j \in \mathcal{A}, \\ 0, \text{ if } j \in \mathcal{A}^c. \end{cases}$$

In addition, with $\boldsymbol{v} = (\boldsymbol{v}_1^\top, \boldsymbol{v}_2^\top)^\top \in \mathbb{R}^{2N}$, we set

$$\boldsymbol{N}(\boldsymbol{v}) := \begin{bmatrix} \boldsymbol{D}(\boldsymbol{v}_1) \ \boldsymbol{D}(\boldsymbol{v}_2) \\ \boldsymbol{D}(\boldsymbol{v}_1) \ \boldsymbol{D}(\boldsymbol{v}_2) \end{bmatrix} \in \mathbb{R}^{2N \times 2N}.$$

In general, the matrix $\boldsymbol{H}^l$ is not symmetric, but at a solution it is symmetric positive definite due to the assumption of the invertibility of $\boldsymbol{M}^*\boldsymbol{M}$. We solve the linear equation in (4) by the biconjugate gradient stabilized (BICGSTAB) algorithm [38]. Similarly to the method [21], the whole algorithm can be shown to converge at a superlinear rate provided that the initial pair $(\boldsymbol{f}^0, \boldsymbol{p}^0)$ is sufficiently close to the solution.

4 Numerical experiments

In this section, we provide numerical results to study the behavior of our method with respect to its image reconstruction capability and its computational efficiency. In our numerics, when solving the primal-dual system (3), unless otherwise specified we set $\gamma = 10^{-3}$, and we stop the semismooth Newton iteration as soon as the initial residual is reduced by a factor of 10^{-3} or after performing 10 semismooth Newton steps. In each semismooth Newton step, the BICGSTAB iteration is stopped as soon as the relative norm of the residual of the primal-dual system (3) at $(\boldsymbol{f}^l, \boldsymbol{p}^l)$ drops below

$$\text{tol}^{l+1} := \frac{1}{10^3} \cdot \min\left\{\left(\frac{\|\boldsymbol{r}^l\|_2}{\|\boldsymbol{r}^0\|_2}\right)^{\frac{3}{2}}, \frac{\|\boldsymbol{r}^l\|_2}{\|\boldsymbol{r}^0\|_2}\right\}, \quad \boldsymbol{r}^l := \begin{pmatrix} \boldsymbol{M}^*\boldsymbol{M}\boldsymbol{f}^l + \text{div}\boldsymbol{p}^l - \boldsymbol{M}^*\boldsymbol{g} \\ \left(\max\{\gamma, |[\nabla\boldsymbol{f}^l]_j|_2\}[\boldsymbol{p}^l]_j + \alpha[\nabla\boldsymbol{f}^l]_j\right)_{j=1,\dots,N} \end{pmatrix}.$$

In order to ensure the invertibility of $\boldsymbol{M}^*\boldsymbol{M}$, as mentioned in the beginning of Section 3, we add a small multiple of the identity matrix and use $\boldsymbol{M}^*\boldsymbol{M} + \kappa_l \boldsymbol{I}_N$ instead. Here, the κ-sequence is generated by $\kappa_{l+1} = 10^{-2}\text{tol}^l$ approaching zero as l increases. Furthermore, for the comparison of computational efficiency, all simulations were performed in MATLAB R2013a on a computer equipped with a Intel Xeon E7450 CPU with 2.4 GHz and 94 GByte main memory. The quality of the reconstructions are shown quantitatively by using the peak signal-to-noise ratio (PSNR) [5], which is a widely used image quality assessment measure.

Example 1. In this example, we give the reconstructed results from the spherical mean values of the phantoms shown in Figure 1 (left) by solving the TV regularization model (P_0). Here, the phantoms are assumed to be supported in the disk with the radius less than 0.5, and there are $M_1 = 80$ detectors (shown as black dots in Figure 1 (left)) uniformly distributed on the surrounding circle. Since in this case the spherical mean values vanish for $r > 1$, the given data $\boldsymbol{g}$, shown in Figure 1 (right), include the spherical mean values with $0 \le r \le 1$, which are discretized at $M_2 = 256$ linearly equally spaced points. Hence, in this example we have $M = 20480$. In addition, the image resolution of the phantoms are 256-by-256, i.e. $N = n^2 = 2^{16}$. In the first row of Figure 2, we show the least squares solutions of (2) by solving $\min_{\boldsymbol{f}} \frac{1}{2}\|\boldsymbol{M}\boldsymbol{f} - \boldsymbol{g}\|_2^2$, which is utilized as the initial value in our method for solving the TV-model.

When solving (P_0) by its locally-smoothed approximation shown in (P), the regularization parameter is set to $\alpha = 10^{-5}$. For the Smiley Face, the semismooth Newton iteration was stopped after 10 iterations with the CPU time 7 hours. And for the Shepp Logan Phantom, the stopping rule of the semismooth Newton iteration was reached after $l = 6$ iterations with the CPU time 13
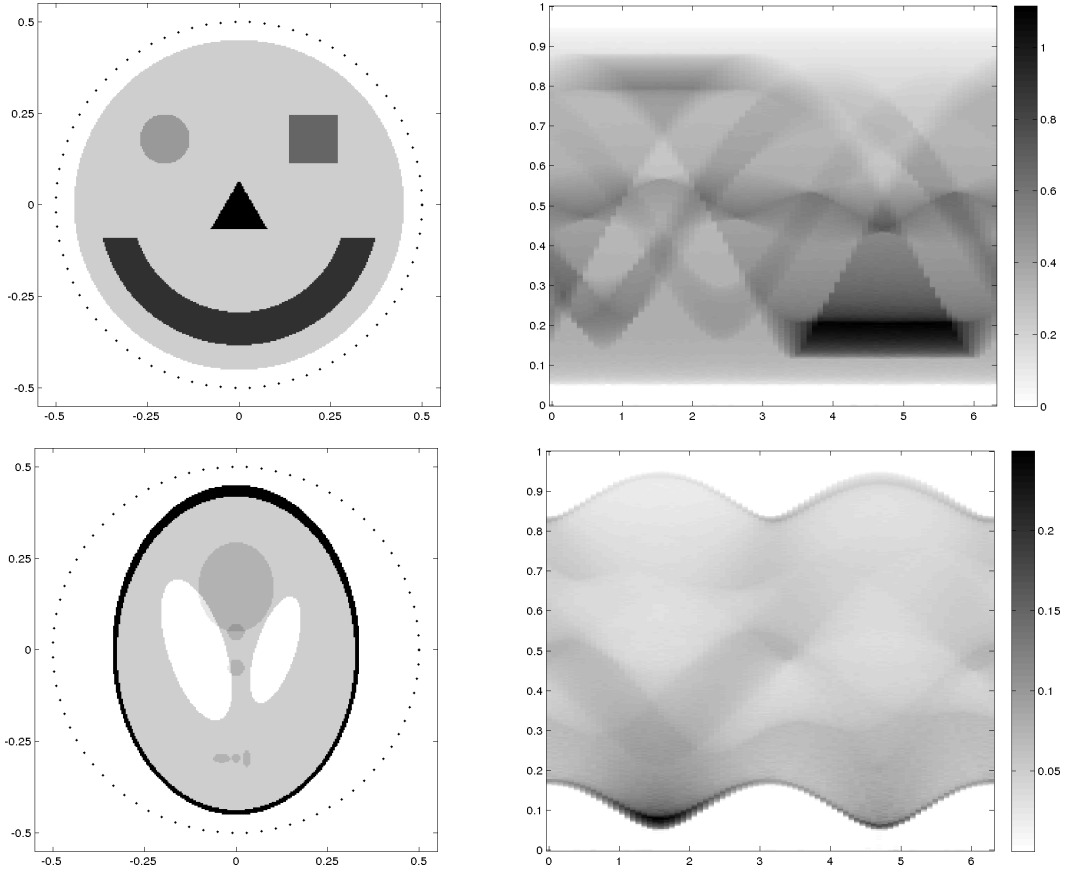
Fig. 1: The phantoms Smiley and Shepp Logan on the left and the data $g \in \mathbb{R}^{M_1 \times M_2}$ on the right.

Table 1: For each iteration l, we show the residual $\|r^l\|_2$ of (3), the objective function value $\mathcal{J}(f)$ of (P_0), and the number of the BICGSTAB iterations l_{inner}.

l	Smiley Face			Shepp Logan Phantom		
	$\|r^l\|_2$	$\mathcal{J}(f^l)$	l_{inner}	$\|r^l\|_2$	$\mathcal{J}(f^l)$	l_{inner}
0	6.14e-1	5.9413	-	1.17e-1	0.2553	-
1	6.67e-3	0.1333	50	2.09e-3	0.0322	50
2	2.52e-3	0.0741	48	6.17e-4	0.0218	50
3	2.93e-3	0.0676	14	4.34e-4	0.0179	50
4	2.53e-3	0.0650	10	2.75e-4	0.0162	50
5	2.57e-3	0.0630	9	1.87e-4	0.0152	50
6	2.34e-3	0.0622	6	1.07e-4	0.0147	50
7	2.58e-3	0.0614	6	–	–	–
8	2.18e-3	0.0608	6	–	–	–
9	2.49e-3	0.0589	9	–	–	–
10	1.83e-3	0.0584	6	–	–	–

hours. Figure 2 (second and third row) shows the reconstructed images after the first and the last iterations. Comparing the final results with the least squares solutions in Figure 2 (first row), we observe that the method based on the TV-model improves the reconstructions visually and quantitatively. Furthermore, to illustrate the convergence behavior of our method for solving (3), in Table 1 we list the residuals of the system (3), the objective function values of (P), and the number of
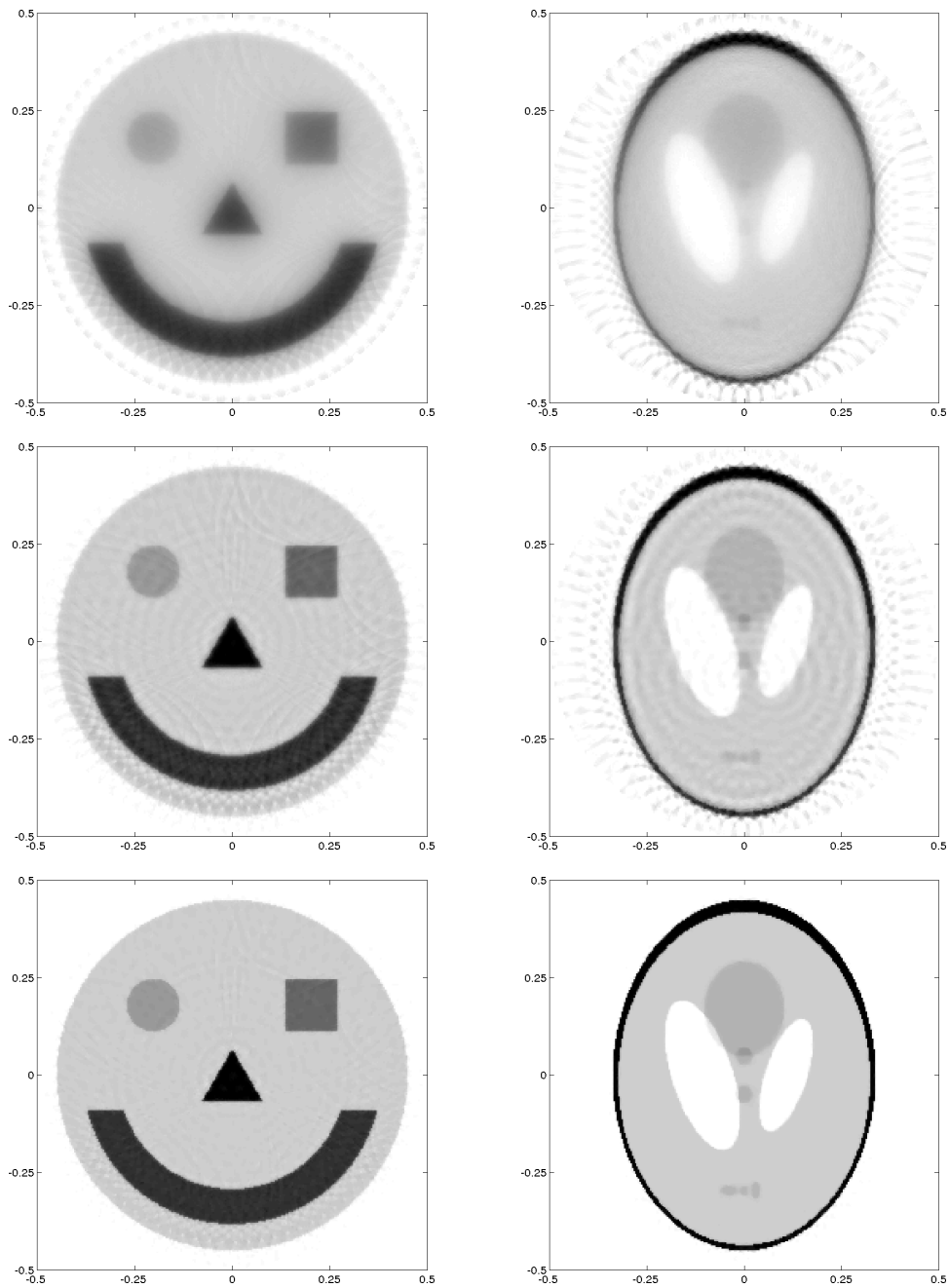
Fig. 2: Reconstructions of the Smiley (left) and the Shepp Logan phantom (right). From top to bottom: The least squares solutions of (2) and the results in the semismooth Newton iterations during solving the TV-model, first and last iteration. The PSNR values are 22.95 dB, 28.73 dB and 33.41 dB on the left and 19.47 dB, 23.04 dB and 34.49 dB on the right.

the BICGSTAB iterations in each semismooth Newton step. The decrease of the residual implies a locally superlinear convergence of the iterations.

The parameter γ in the Huber function Φ_γ in (P) controls the balance between the quadratic regularization and the TV regularization. By comparing the PSNR values and additional visual inspection in numerical experiments, we observed that small γ provides sharper edges in the reconstructed result due to the TV regularization, and large γ oversmooths the edges due to the quadratic regularization. Furthermore, large γ accelerates the numerical computation. In addition, based on Theorem 1, the solution of (P) converges to the one of (P_0) as γ tends to zero. While decreasing γ during the iterations only mildly improves the result and does not speed up the computations in the numerical experiments, we keep a fixed parameter $\gamma = 10^{-3}$ in the following examples.

Example 2. In order to show the computational efficiency, we compare our primal-dual method combined with the semismooth Newton technique with another accelerated first-order primal-dual method proposed in [8], which is also able to solve the locally-smoothed TV-model in (P). To compare the computational efficiency, Figure 3 (left) shows the plots of the objective function values of (P) versus iterations with the same $\alpha = 10^{-5}$ and $\gamma = 10^{-3}$. For our method, except the total 10 Newton iterations, the inner iterations for solving the linear equation in (4) are also counted, i.e., the difference of the number of iterations between two Newton steps equals to the number of the inner iterations of the BICGSTAB algorithm, see Table 1. In this example, we stop the first-order primal-dual method proposed in [8] after 1000 iterations having spent 23 hours CPU time. The final function value is still larger than that from our method after 10 semismooth Newton iterations and a CPU time of 9 hours. We conclude that our method is more efficient in this situation. In addition, we also give the reconstructed images obtained by both methods. Since the first-order primal-dual method (middle) in [8] and our method (right) both aim at minimizing the locally-smoothed TV-model (P), they obtain similar results. But comparing the reconstructions of smiley phantom, we can see that some corners are smoothed in the result from the method in [8], and our method performs a more exact reconstruction. This difference is due to the accuracy of the calculations. If we increase the number of the iterations in the method from [8], a similar reconstruction quality can be reached by spending more CPU-time.
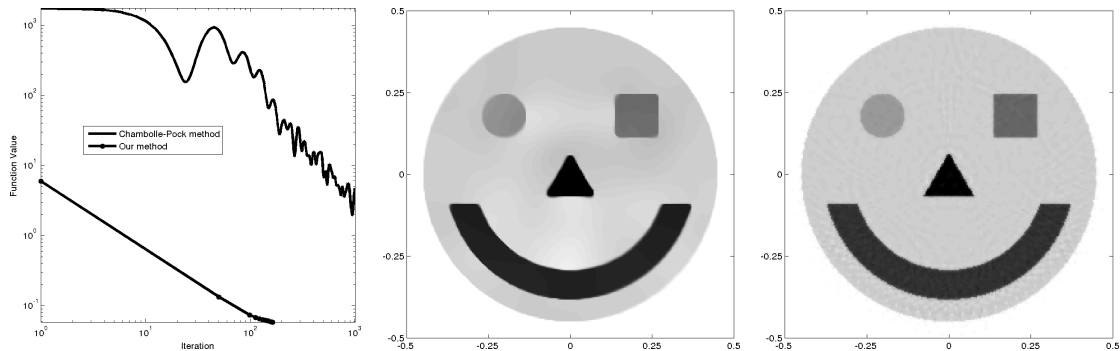

Fig. 3: The objective function values of (P) versus inner iterations for the primal-dual method [8] (PSNR = 28.34 dB) and our method (PSNR = 33.41 dB).

Example 3. Now, we test our method for reconstructing from data corrupted by white Gaussian noise with different noise levels, see Figure 4. The results obtained by solving the least squares problem $\min_{\boldsymbol{f}} \|\boldsymbol{M}\boldsymbol{f} - \boldsymbol{g}\|_2^2$ and our method for solving the TV-model (P_0) are shown in Figure 5. Since the parameter α controls the trade-off between a good fit to $\boldsymbol{g}$ and a smoothness requirement due to the TV regularization, we list two results with different values of α for each noise level. It is seen that with larger α, the reconstructed images are smoother, and more noise is removed; however, with smaller α the results include more details, but at the same time some noise is left; see, e.g., the right eye and the cheek of the phantom. This also suggests that small α is used for low noise level in order to preserve details with little smoothing, and large α is used for high noise level in order to

remove most noise. In addition, since the TV regularization is utilized in our method, it leads to the well known staircasing effect; see, e.g., the cheek of the phantom.
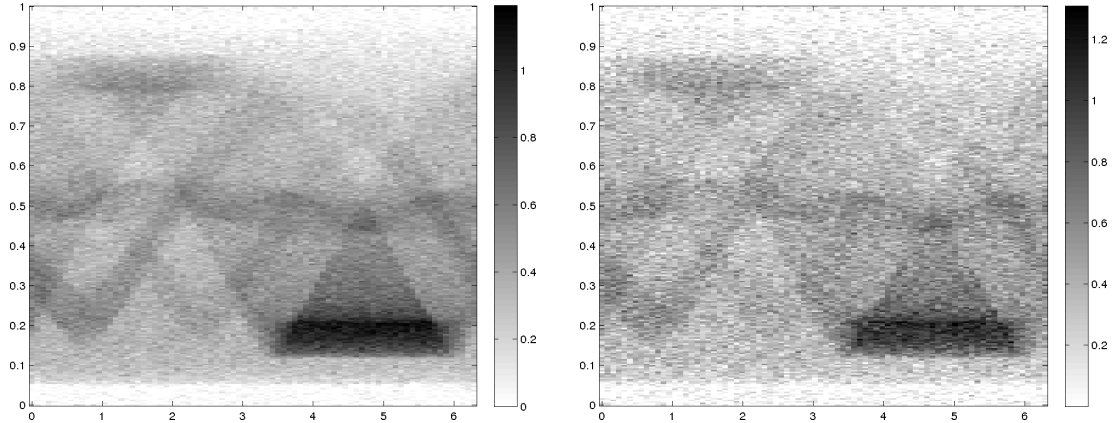

Fig. 4: The data g with white Gaussian noise, left: 5% noise, PSNR = 26.09 dB; right: 10% noise, PSNR = 20.07 dB.

Table 2: For different noise levels and α, the number of semismooth Newton iterations l^{all}, the total number of the BICGSTAB iterations $l^{\mathrm{all}}_{\mathrm{inner}}$, and the CPU time t.

noise	5%		10%	
α	0.01	0.006	0.02	0.01
l^{all}	10	10	10	10
$l^{\mathrm{all}}_{\mathrm{inner}}$	447	441	355	457
t	23 h	21 h	16 h	20 h

In Table 2 we list the number of the semismooth Newton iterations, the total number of the BICGSTAB iterations, and the CPU time. Although in all our tests the numbers of semismooth Newton steps reach the maximum of 10 iterations, the reconstructed results are already acceptable. Based on our numerical experiments, allowing more iterations yields no significant effect on the results.

Example 4. Since in many practical cases the detectors are only able to be located on a limited region, in this last example we consider detectors uniformly distributed on a J-shape as depicted in Figure 6. Here a so-called visibility condition is violated and thus the reconstruction problem is severely ill-posed, see e.g. [25] for a detailed discussion. We show the data g and the reconstructed image by our algorithm based on the TV-model with $\alpha = 10^{-4}$. We note that in this limited view case solving the TV-model by our primal-dual method still gives a good reconstruction with a PSNR = 33.67 dB but of course also shows some blurring artifacts e.g. at the right corner of the mouth.

5 Summary

We introduced a novel iterative reconstruction method in photoacoustic imaging which does not rely on a specific geometry of the detectors. Based on a dedicated discretization of the spherical mean value operator and a total variation regularizer, our method performs reasonable efficiently and preserves important features like edges in the reconstruction.

(a) PSNR = 21.42 dB

(b) PSNR = 18.41 dB

(c) $\alpha = 0.01$, PSNR = 24.15 dB

(d) $\alpha = 0.02$, PSNR = 23.28 dB

(e) $\alpha = 0.006$, PSNR = 25.51 dB
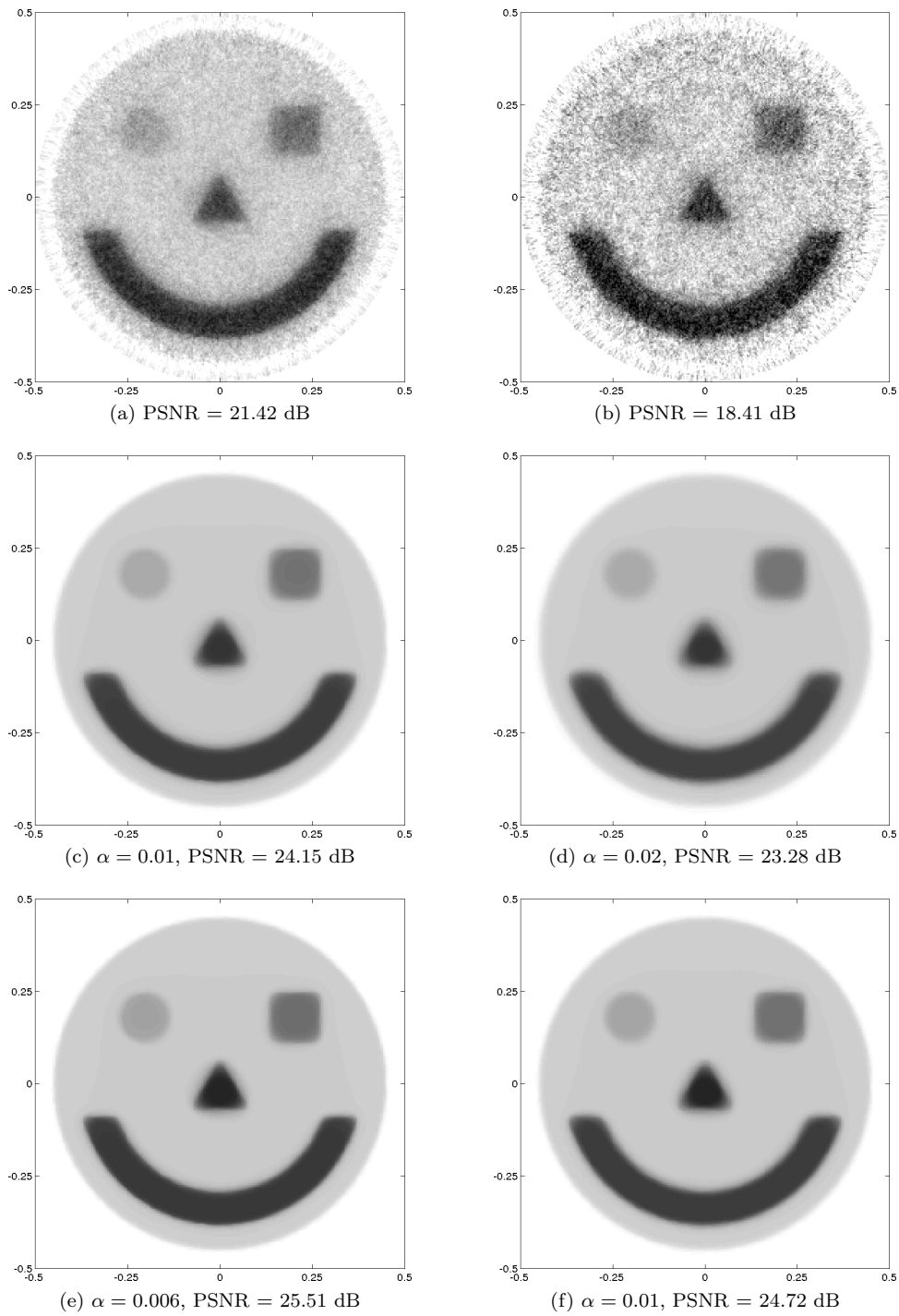
(f) $\alpha = 0.01$, PSNR = 24.72 dB

Fig. 5: The reconstructed results by solving the least squares problem and our TV-model with different parameter values and data noise levels, 1st column: 5% noise; 2nd column: 10% noise.
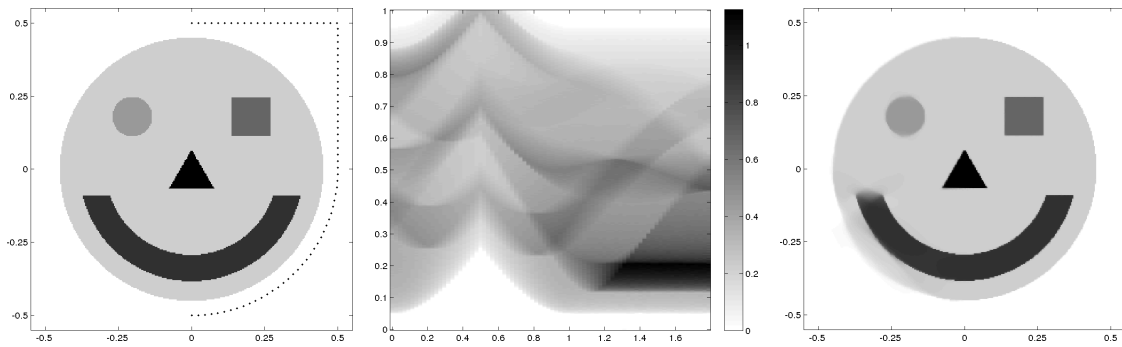
Fig. 6: From left to right: The phantom and detector positions, the data $\boldsymbol{g}$, and the result by solving (P_0).

References

1. M. Agranovsky and P. Kuchment. Uniqueness of reconstruction and an inversion procedure for thermoacoustic and photoacoustic tomography with variable sound speed. *Inverse Problems*, 23(5):2089–2102, 2007.
2. M. Agranovsky, P. Kuchment, and L. Kunyansky. On reconstruction formulas and algorithms for the thermoacoustic tomography. In L. V. Wang, editor, *Photoacoustic imaging and spectroscopy*, chapter 8, pages 89–101. CRC Press, Boca Raton, FL, 2009.
3. M. Agranovsky, P. Kuchment, and E. T. Quinto. Range descriptions for the spherical mean Radon transform. *J. Funct. Anal.*, 248(2):344–386, 2007.
4. M. Ansorg, F. Filbir, W. R. Madych, and R. Seyfried. Summability kernels for circular and spherical mean data. *Inverse Problems*, 29(1):015002, 2013.
5. A. Bovik. *Handbook of Image and Video Processing*. Academic Press, 2000.
6. A. Buehler, A. Rosenthal, T. Jetzfellner, A. Dima, D. Razansky, and V. Ntziachristos. Model-based optoacoustic inversions with incomplete projection data. *Med. Phys.*, 38(1694), 2011.
7. P. Burgholzer, G. J. Matt, M. Haltmeier, and G. Paltauf. Exact and approximate imaging methods for photoacoustic tomography using an arbitrary detection surface. *Phys. Rev. E*, 75(4):046706, 2007.
8. A. Chambolle and T. Pock. A first-order primal-dual algorithm for convex problems with applications to imaging. *J. Math. Imaging Vision*, 2011.
9. R. Courant and D. Hilbert. *Methods of mathematical physics. Vol. II: Partial differential equations. (Vol. II by R. Courant.)*. Interscience Publishers (a division of John Wiley & Sons), New York-London, 1962.
10. F. Filbir, R. Hielscher, and W. R. Madych. Reconstruction from circular and spherical mean data. *Appl. Comput. Harmon. Anal.*, 29(1):111–120, 2010.
11. D. Finch, M. Haltmeier, and Rakesh. Inversion of spherical means and the wave equation in even dimensions. *SIAM J. Appl. Math.*, 68(2):392–412, 2007.
12. T. Görner, R. Hielscher, and S. Kunis. Efficient and accurate computation of spherical mean values at scattered center points. *Inverse Probl. Imaging*, 6(4):645–661, 2012.
13. M. Haltmeier. A mollification approach for inverting the spherical mean Radon transform. *SIAM J. Appl. Math.*, 71(5):1637–1652, 2011.
14. M. Haltmeier. Universal inversion formulas for recovering a function from spherical means. *ArXiv e-prints*, 2012.

15. M. Haltmeier. Inversion of circular means and the wave equation on convex planar domains. *Comput. Math. Appl.*, 65(7), 2013.
16. M. Haltmeier, O. Scherzer, P. Burgholzer, and G. Paltauf. Thermoacoustic computed tomography with large planar receivers. *Inverse Problems*, 20(5):1663–1673, 2004.
17. M. Haltmeier, O. Scherzer, and G. Zangerl. A reconstruction algorithm for photoacoustic imaging based on the nonuniform FFT. *IEEE Trans. Med. Imag.*, 28(11):1727–1735, 2009.
18. M. Haltmeier, T. Schuster, and O. Scherzer. Filtered backprojection for thermoacoustic computed tomography in spherical geometry. *Math. Methods Appl. Sci.*, 28(16):1919–1937, 2005.
19. M. Haltmeier and G. Zangerl. Spatial resolution in photoacoustic tomography: effects of detector size and detector bandwidth. *Inverse Problems*, 26(12):125002, 14, 2010.
20. M. Hintermüller, K. Ito, and K. Kunisch. The primal-dual active set strategy as a semismooth Newton method. *SIAM J. Optim.*, 13(3):865–888 (2003), 2002.
21. M. Hintermüller and G. Stadler. An infeasible primal-dual algorithm for total bounded variation-based inf-convolution-type image restoration. *SIAM J. Sci. Comput.*, 28(1):1–23, 2006.
22. Y. Hristova, P. Kuchment, and L. Nguyen. Reconstruction and time reversal in thermoacoustic tomography in acoustically homogeneous and inhomogeneous media. *Inverse Problems*, 24(5):055006, 25, 2008.
23. P. J. Huber. Robust regression: asymptotics, conjectures and Monte Carlo. *Ann. Statist.*, 1:799–821, 1973.
24. J. Keiner, S. Kunis, and D. Potts. Using NFFT 3—a software library for various nonequispaced fast Fourier transforms. *ACM Trans. Math. Software*, 36(4):Art. 19, 30, 2009.
25. P. Kuchment and L. Kunyansky. Mathematics of thermoacoustic tomography. *European J. Appl. Math.*, 19(2):191–224, 2008.
26. S. Kunis and I. Melzer. A stable and accurate butterfly sparse Fourier transform. *SIAM J. Numer. Anal.*, 50(3):1777–1800, 2012.
27. L. Kunyansky. Reconstruction of a function from its spherical (circular) means with the centers lying on the surface of certain polygons and polyhedra. *Inverse Problems*, 27(2):025012, 22, 2011.
28. L. A. Kunyansky. Explicit inversion formulae for the spherical mean Radon transform. *Inverse Problems*, 23(1):373–383, 2007.
29. L. A. Kunyansky. A series solution and a fast algorithm for the inversion of the spherical mean Radon transform. *Inverse Problems*, 23(6):S11–S20, 2007.
30. F. Natterer. Photo-acoustic inversion in convex domains. *Inverse Probl. Imaging*, 6(2):1–6, 2012.
31. Y. Nesterov. Smooth minimization of non-smooth functions. *Math. Program.*, 2005.
32. V. Palamodov. Remarks on the general funk transform and thermoacoustic tomography. *Inverse Probl. Imaging*, 4:693 – 702, 2010.
33. G. Paltauf, R. Nuster, M. Haltmeier, and P. Burgholzer. Photoacoustic tomography with integrating area and line detectors. In L. V. Wang, editor, *Photoacoustic Imaging and Spectroscopy*, Optical Science and Engineering, chapter 20, pages 251–263. CRC Press, Boca Raton, FL, 2009.
34. L. Q. Qi and J. Sun. A nonsmooth version of Newton's method. *Math. Programming*, 58(3, Ser. A):353–367, 1993.
35. J. Qian, P. Stefanov, G. Uhlmann, and H. Zhao. An efficient Neumann series-based algorithm for thermoacoustic and photoacoustic tomography with variable sound speed. *SIAM J. Imaging Sci.*, 4(3):850–883, 2011.
36. E. T. Quinto. Helgason's support theorem and spherical Radon transforms. In *Radon transforms, geometry, and wavelets*, volume 464 of *Contemp. Math.*, pages 249–264. Amer. Math. Soc., Providence, RI, 2008.
37. L. Rudin, S. Osher, and E. Fatemi. Nonlinear total variation based noise removal algorithms. *Physica D*, 60:259–268, 1992.
38. Y. Saad. *Iterative methods for sparse linear systems.* Society for Industrial and Applied Mathematics, Philadelphia, PA, second edition, 2003.
39. P. Stefanov and G. Uhlmann. Thermoacoustic tomography with variable sound speed. *Inverse Problems*, 25(7):075011, 16, 2009.
40. L. V. Wang and H. Wu. *Biomedical Optics - Principles and Imaging.* John Wiley & Sons Inc., Hoboken, NJ, 2007.

41. L. Ying. Sparse Fourier transform via butterfly algorithm. *SIAM J. Sci. Comput.*, 31(3):1678–1694, 2009.
42. G. Zangerl and O. Scherzer. Exact reconstruction in photoacoustic tomography with circular integrating detectors II: spherical geometry. *Math. Methods Appl. Sci.*, 33(15):1771–1782, 2010.
43. G. Zangerl, O. Scherzer, and M. Haltmeier. Exact series reconstruction in photoacoustic tomography with circular integrating detectors. *Commun. Math. Sci.*, 7(3):665–678, 2009.